Fast Single Image Defogging With Robust Sky Detection

**SEBASTIÁN SALAZAR-COLORES[1], E. ULISES MOYA-SÁNCHEZ [2,3], (Member, IEEE),
JUAN-MANUEL RAMOS-ARREGUÍN [4], (Senior Member, IEEE),
EDUARDO CABAL-YÉPEZ [5], (Member, IEEE), GERARDO FLORES [1], (Member, IEEE),
AND ULISES CORTÉS[6,7]**

[1]Centro de Investigaciones en Óptica, A.C., León 37150, México
[2]Coordinación General de Innovación Gubernamental, Gobierno del estado de Jalisco, Guadalajara 44100, México
[3]Maestría en Ciencias Computacionales, Universidad Autónoma de Guadalajara, Zapopan 45129, México
[4]Facultad de Ingeniería, Universidad Autónoma de Querétaro, Querétaro 76000, México
[5]Departamento de Estudios Multidisciplinarios, División de Ingenierías, Universidad de Guanajuato, Yuriria 38944, México
[6]Computer Science Department, Universitat Politècnica de Catalunya (Barcelona Tech), 08034 Barcelona, Spain
[7]High-Performance Artificial Intelligence Group, Barcelona Supercomputing Center, 08034 Barcelona, Spain

Corresponding author: E. Ulises Moya-Sánchez (eduardo.moya@jalisco.gob.mx)

ABSTRACT Haze is a source of unreliability for computer vision applications in outdoor scenarios, and it is usually caused by atmospheric conditions. The Dark Channel Prior (DCP) has shown remarkable results in image defogging with three main limitations: 1) high time-consumption, 2) artifact generation, and 3) sky-region over-saturation. Therefore, current work has focused on improving processing time without losing restoration quality and avoiding image artifacts during image defogging. Hence in this research, a novel methodology based on depth approximations through DCP, local Shannon entropy, and Fast Guided Filter is proposed for reducing artifacts and improving image recovery on sky regions with low computation time. The proposed-method performance is assessed using more than 500 images from three datasets: Hybrid Subjective Testing Set from Realistic Single Image Dehazing (HSTS-RESIDE), the Synthetic Objective Testing Set from RESIDE (SOTS-RESIDE) and the HazeRD. Experimental results demonstrate that the proposed approach has an outstanding performance over state-of-the-art methods in reviewed literature, which is validated qualitatively and quantitatively through Peak Signal-to-Noise Ratio (PSNR), Naturalness Image Quality Evaluator (NIQE) and Structural SIMilarity (SSIM) index on retrieved images, considering different visual ranges, under distinct illumination and contrast conditions. Analyzing images with various resolutions, the method proposed in this work shows the lowest processing time under similar software and hardware conditions.

INDEX TERMS Dark channel prior, defogging, image enhancement, single image dehazing, sky detection.

I. INTRODUCTION

Fog or haze is a major source of unreliability in outdoor navigation systems, surveillance systems, and other outdoor computer vision applications, which usually is caused by atmospheric conditions [1]–[3]. Defogging can be defined as the removal of fog. Defogging algorithms have to deal with a trade-off between restoration quality, under different fog intensities and scenarios [4], [5], and time-consumption [1], [6].

The associate editor coordinating the review of this manuscript and approving it for publication was Jiachen Yang.

He *et al.* [7] proposed the use of Dark Channel Prior (DCP) in defogging tasks, which demonstrated that it is possible to remove fog with remarkable results [7]. Nevertheless, DCP has three inherent limitations: 1) high time-consumption, 2) artifact generation, and 3) sky-region over-saturation [8], [9]. Recent research has focused on reducing DCP processing time without losing restoration quality, and avoiding image artifacts [6], [10]. For instance, Pang *et al.* [11] used the DCP and the Guided Filter to avoid image artifacts by refining the obtained transmission map. Zhu and He [10] improved the image restoration by minimizing the energy function through a linear attenuation based on saturation and

brightness. Nishino *et al.* [12]employed the maximum posterior probability to compute image depth more accurately. Recently, pixel clustering in the RGB space was used to reduce image artifacts during image defogging assuming that colors in a haze-free image are closely approximated by a few hundreds of distinct colors [13]. Furthermore, some optimization approaches have been proposed for obtaining enhanced dehazing results [14], [15]. For instance, some methods based on Artificial Intelligence (AI) have yielded to promising results through the use of a Multilayer Perceptron (MLP) [16]. On the other hand, Ren *et al.* [17] used a multi-scale Convolutional Neural Network (CNN), a coarse-scale net to predicts a transmission map, and a fine-scale net to locally refine results. Cai *et al.* [18] proposed the DehazeNet that adopts the CNN deep architecture specially designed to embody image dehazing. Li *et al.* [19] proposed an end-to-end CNN based design (AOD-Net) for improving high-level tasks on hazy images. In [20], an image-to-image translation problem was proposed using a generative adversarial network, named Enhanced Pix2pix Dehazing Network, to generate a haze-free image (without the physical scattering model). Fu *et al.* [21] employed a convolutional network architecture, called multi-feature-based bilinear CNN, to mitigate halo effects, abrupt edges, and image noise. However, despite the progress in AI-based methods, DCP-based research has continued [22]. For example [8], [9], [23]–[26] are focused on reducing the over-saturated areas generated when DCP is applied over sky regions. These works improved DCP computation by adding an image segmentation stage or implementing quadtree techniques, but their main drawback is the relatively long processing time. Furthermore, research efforts have focused on improving the performance measurement of dehazing methods [1], [27]–[29]. The main difference of the method proposed in this work regarding previous dehazing DCP/Fast Guided Filter (FGF) [5], [7], [30], [31] and sky-detection based methods [8], [9], [23]–[25] is the effective combination of DCP and FGF with local Shannon entropy, resulting in a fast and efficient method with remarkable results on outdoor-image dehazing.

This research aims to recover the latent sharp image from its hazy version, overcoming the DCP limitations. The proposed-method main contributions are:

- The improved performance of existing dark channel prior (DCP) dehazing algorithms based on a robust sky-detection-segmentation and the Fast Guided Filter.
- A robust sky-detection-segmentation process, based on DCP and local Shannon entropy.
- Faster computation speed and competitive performance than recent deep learning based dehazing algorithms under similar conditions of software and hardware.

As a result, the proposed method reduces typical DCP artifacts, achieving a better recovery on sky regions than the techniques in reviewed literature, reducing over-saturated areas, and reaching a proper response with an adequate trade-off between different levels of haze and computation time.

Quality of defogged images obtained from the proposed methodology is analyzed through qualitative and quantitative metrics commonly used in literature about this subject [5], [9], [17], [32]. The quantitative evaluation is conducted using Peak Signal-to-Noise Ratio (PSNR), Naturalness Image Quality Evaluator (NIQE) and Structural SIMilarity (SSIM) index. More than 500 images are used, based on both synthetic and real hazy images, from three datasets: the Hybrid Subjective Testing Set from Realistic Single Image Dehazing (HSTS-RESIDE) [33], the Synthetic Objective Testing Set from RESIDE (SOTS-RESIDE) [33], and the HazeRD (with different levels of visibility due to fog) [34]. The proposed method is compared against nine state-of-art single image defogging methods[1]: He *et al.* [7], Pang *et al.* [11], Zhu and He [10] Berman *et al.* [13], Ren *et al.* [17], Cai *et al.* [18], Li *et al.* [19], Qu *et al.* [20], and Salazar-Colores *et al.* [16].

Obtained results and performed analyses demonstrate that the proposed method improves the image recovery process by reducing the typical DCP artifacts, minimizing over-saturated areas and generating a robust response to different levels of haze with less computation time.

The remaining of the document is organized as follows: Section II introduces the theoretical background of involved topics. Section III is devoted to the proposed method and used data. Obtained results and their corresponding analysis are presented in Section IV. Finally, some conclusions are given in Section V.

II. BACKGROUND
A. ATMOSPHERIC DICHROMATIC MODEL

Image-degradation by haze is caused because of particles in the atmospheric medium absorb and scatter light [35]. The most accepted model for atmospheric degradation can be expressed as follows [35]:

$$y_i = t_i x_i + (1 - t_i)a, \qquad (1)$$

where $y_i \in \mathbb{R}^3$ represents the RGB foggy or haze image, $x_i \in \mathbb{R}^3$ is the RGB fog-free (sharp) image, $t_i \in \mathbb{R}$ is the transmission medium, $i \in \mathbb{N}$ represents the pixel position of each variable, and $a \in \mathbb{R}^3$ represents the atmospheric light color. Assuming that the wavelength is independent of the atmospheric scattering, the transmission t_i can be expressed as follows [35]:

$$t_i = e^{-\beta d_i}, \qquad (2)$$

where β is a homogeneous attenuation coefficient and d_i is the scene depth at each pixel i.

Based on (1), it is possible to retrieve an estimate $\hat{x}_i$ of the fog-free image x_i from the foggy image y_i as follows [35]:

$$\hat{x}_i = \frac{y_i - a}{t_i} + a, \qquad (3)$$

---

[1]Note that some of these methods use state-of-the-art techniques such as deep learning and generative models.

DCP is one of the most widely-used methods for computing these unknown variables t_i and a in order to dehaze the image [7], [36].

B. THE DARK CHANNEL PRIOR

The dark channel of image y_i is defined as [36]

$$dc_i = \min_{i \in \Omega_k} \min_{c \in \{r,g,b\}} \left(\frac{y_i^c}{a^c} \right), \qquad (4)$$

where the c-th color component of y_i and a are y_i^c and a^c respectively, Ω_k is a square patch of size $s \times s$ centered in a pixel k.

According to [36] and [35], it is possible to establish the relation between a fog-free image and its dark channel. For the case of non-sky regions, the dark channel usually has low-intensity values , i. e.

$$dc_i \to 0. \qquad (5)$$

From the previously established relation, He *et al.* [7] proposed that the corresponding transmission t_i can be computed as

$$t_i = 1 - \omega dc_i, \qquad (6)$$

where $0 \leq \omega \leq 1$ is the level of the desired restoration. The atmospheric light color a is computed by selecting the brightest pixel of y_i, from the subset of dc_i composed of the 0.1% of the brightest values.

1) RELATION BETWEEN dc_i AND DEPTH d_i

Substituting (2) in (6), with $w = 1$ we can establish the relation between dc_i and d_i as

$$dc_i = 1 - e^{-\beta d_i}, \qquad (7)$$

as a consequence, when the distance $d_i \to 0$, $dc_i = 0$, and when $d_i \to \infty$, $dc_i = 1$.

DCP-based methods usually have two main drawbacks [1]:

1) Generation of saturated sky-regions i.e. sky regions with unreal colors as shown in Fig. 1(c).
2) The restoration or recovery process has a trade-off between the retrieved-image quality (produced number of artifacts) and processing time. Fig. 1(d) shows an example of the visual artifacts that can be generated.

C. LOCAL SHANNON ENTROPY

The local Shannon entropy E_{Ω_k} on a square window Ω_k is defined as

$$E_{\Omega_k} = -\sum_{j=0}^{L-1} P_j \log P_j, \qquad (8)$$

where L is the number of possible values for a pixel of E_{Ω_k} (in a grey-scale image L equal to 256), $P_j = \frac{n_j}{s \times s}$ is the probability that the grey-scale value j appears in Ω_k, which is an $s \times s$ square window centered in the pixel k. n_j is the number of pixels with the value j in Ω_k.
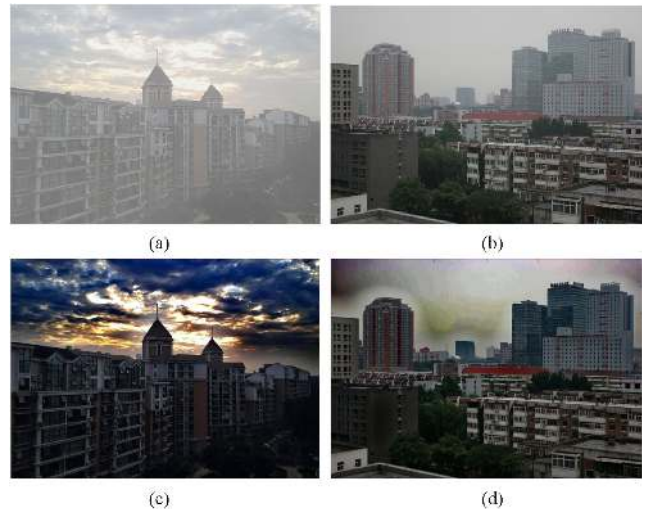

FIGURE 1. Examples of the main drawbacks of DCP method. (a) Input image 1, (b) input image 2, (c) restored image from (a) presenting saturated sky regions, (d) restored image from (b) illustrating image artifacts.

D. THE FAST GUIDED FILTER

The Fast Guided Filter (FGF) [30] is an edge-preserving linear smoothing filter defined as

$$q_i = a_k I_i + b_k, \quad \forall i \in \Omega_k, \qquad (9)$$

where q_i is the filtering output image and I_i is the guidance image. i is the position of a pixel and k is the index of a local square window Ω with size $s \times s$. a_k and b_k are linear coefficients constants in Ω_k. Given the filtering input image p, the filter minimizes the reconstruction error between p and q as

$$a_k = \frac{\frac{1}{|\omega|} \sum_{i \in \omega_k} I_i p_i - \mu_k \hat{p}_k}{\sigma_k^2 + \epsilon}, \qquad (10)$$

$$b_k = \hat{p}_k - a_k \mu_k, \qquad (11)$$

where μ_k and σ_k are the mean and variance of I in Ω_k, $\hat{p}_k$ is the average of p in Ω_k, and ϵ is a regularization parameter controlling the degree of smoothness.

III. METHODS AND DATA

A. PROPOSED METHOD

The proposed method is based on two assumptions about sky regions in hazy outdoor images:

1) Sky region distance $d_i \to \infty$ from the capture device; thus, the transmission t_i described in (2) takes the value $t_i = e^{-\infty}$, i.e., $t_i \to 0$. Based on (7), it can be concluded that dark channel $dc_i \to 1$ in sky regions, as shown in Fig. 2(c).
2) Sky regions are mainly homogeneous; hence, the local Shannon entropy E_{Ω_k}, computed over the magnitude of gradient e_i in homogeneous regions, has low values, i.e., $E_{\Omega_k} \to 0$ [37]. Fig. 2(d) depicts the local Shannon entropy map, where it is possible to see how the sky region values tend to zero in the entropy map.
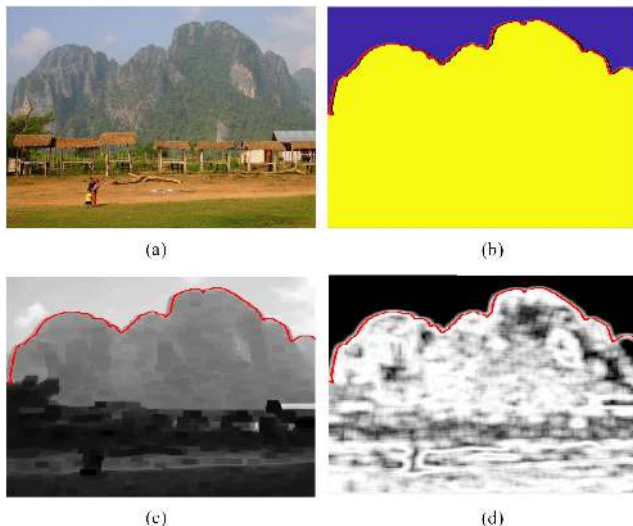
FIGURE 2. (a) Input image, (b) ground truth segmented sky, (c) dark channel intensity map, where $dc_i \to 1$ in the sky region, and (d) local Shannon entropy map, where $E(\Omega_k) \to 0$ in the sky region.

Based on these two assumptions, a new two-stages method that computes an initial and an improved dark channel maps, is proposed. The aim of the first stage is to compute initial values of dc_i^0, a^0, and sky region mask s_i. The second stage is devoted to obtain an improved dark channel map dc_i^1, atmospheric light a^1, and a refined transmission map t_i^1 using the sky detection-segmentation. Fig. 3 presents a flowchart of the proposed method, and Fig. 4 provides an stage-to-stage visual example of its application. The detection and segmentation of sky regions are explained in Section III-B. Each stage of the proposed method is detailed as follows:

- **Stage 1**. From an input image y_i, Fig. 4(a), it is possible to obtain its corresponding dark channel dc_i^0 with an initial atmospheric light a^0 and a sky mask s_i as follows:

  1) Estimate the atmospheric light a^0 as in [36], Fig. 4(b).
  2) Compute the dark channel dc_i^0 using a^0 and (4), Fig. 4(c).
  3) Detect, segment, and obtain the sky region mask s_i using local Shannon entropy and dark channel criteria described in Section III-B, Fig. 4(d).

- **Stage 2**. Compute an improved atmospheric light a^1 and transmission map t_i^1 by using the detected sky region s_i. Finally, apply the scattering model as follows:

  4) Estimate the atmospheric light a^1 based on the detected sky region s_i, as the average of the pixels in the input image y_i that belong to the sky region s_i. If a sky region is not detected, the value of a^1 is assigned as $a^1 = [1 \ \ 1 \ \ 1]$, as shown in Fig. 4(e).
  5) Compute dark channel dc_i^1 using a^1 and (4), as shown in Fig. 4(f).
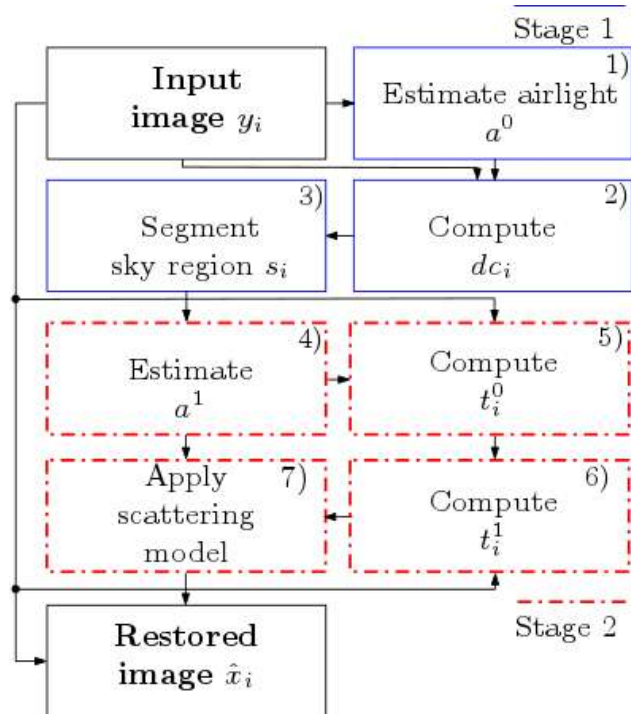

FIGURE 3. Flowchart of the two-stages proposed method.
Stage 1 computes the initial transmission map and the atmospheric light (blue line boxes). Stage 2, improves the transmission map using the sky detection-segmentation (red dot-line boxes).

6) Compute a rough transmission t_i^0 based on the dark channel dc_i^1 as follows:

$$t_i^0 = 1 - \omega \begin{cases} 1 - dc_i^1, & \text{if } s_i = 1 \text{ (sky)} \\ dc_i^1, & \text{otherwise.} \end{cases} \quad (12)$$

Please refer to Fig. 4(g).

7) Compute a final refined transmission t_i^1 using the FGF (see Section II-D) as follows:

$$t_i^1 = \text{FGF}(y_i, t_i^0). \quad (13)$$

Please refer to Fig. 4(h).

8) Retrieve the restored image $\hat{x}_i$ by applying the scattering model using the refined transmission map t_i^1 and the atmospheric light a^1 through (3), as shown in Fig. 4(i).

B. SKY REGION DETECTION-SEGMENTATION

The sky detection-segmentation flowchart process is presented in Fig. 5.[2] This process is divided into two stages: detecting and segmenting a baseline sky region, and refining or improving the sky region, as depicted in Fig. 6. The stages of this process are described as follows:

- Stage 1. Detect and segment a baseline sky region.

  1) The input image y_i is transformed from its RGB color model into the corresponding CIELab color

---

[2] To obtain a better performance, the sky detection-segmentation is performed over a scaled version of the image (600×400 pixels).
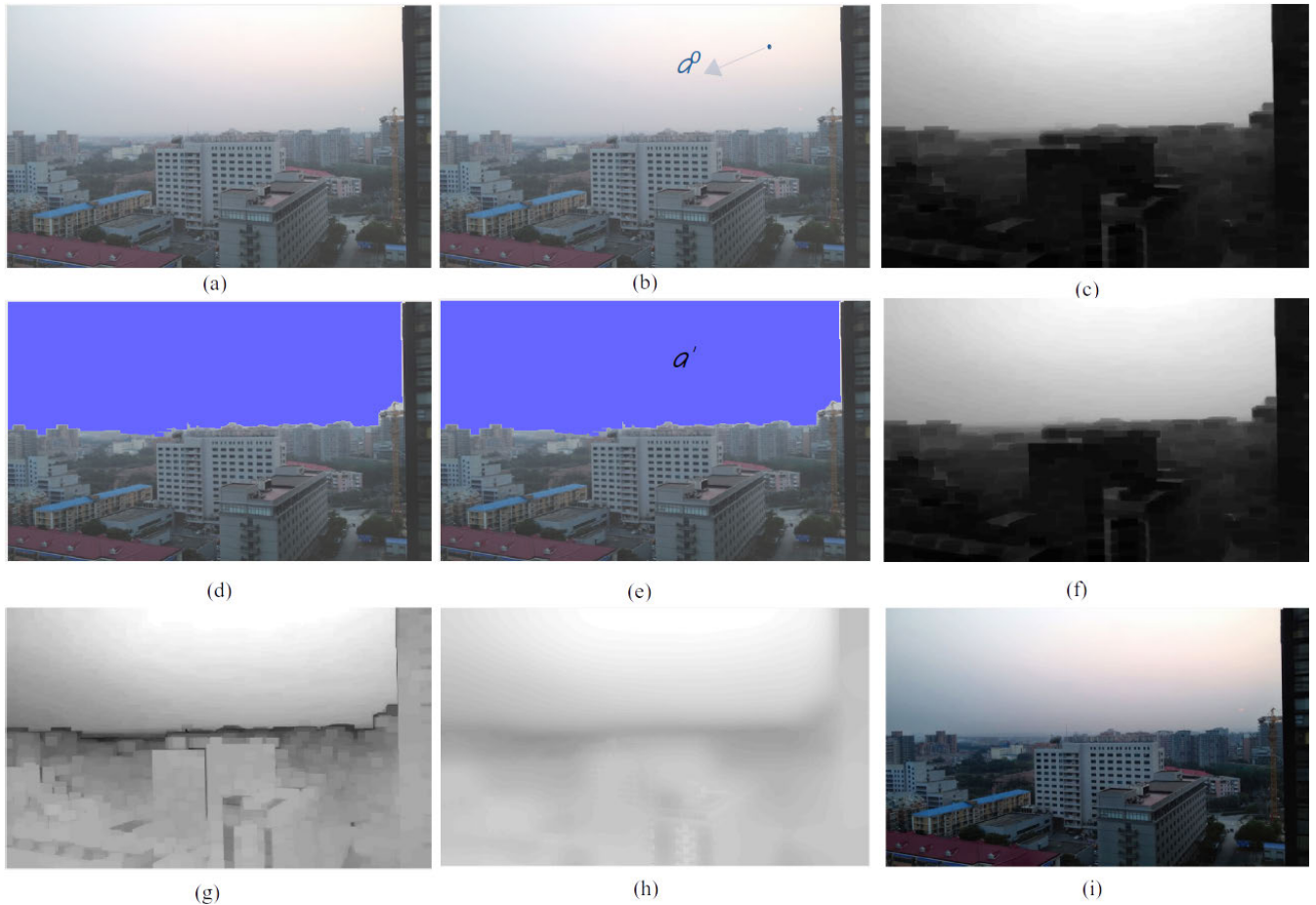
FIGURE 4. Proposed method. (a) Input image, (b) estimated atmospheric light a^0, (c) computed dark channel dc_i^0, (d) segmented sky region s_i, (e) improved atmospheric light a^i estimation, (f) computed dark channel dc_i^1, (g) rough transmission map t_i^0, (h) refined transmission map t_i^1, (i) recovered image $\hat{x}$.

space $\bar{y}_i$ in order to obtain an accurate gradient information [38].

2) The gradient magnitude G_i is computed over the Luminance (L) channel $\bar{y}_i(1)$, as shown Fig. 6 (b).

$$G_i = \sqrt{\mathbf{Gx_i}^2 + \mathbf{Gy_i}^2}, \qquad (14)$$

where $\mathbf{Gx_i}$, $\mathbf{Gy_i}$ are the Sobel operators, defined as:

$$\mathbf{Gx_i} = \begin{bmatrix} -1 & 0 & 1 \\ -2 & 0 & 2 \\ -1 & 0 & 1 \end{bmatrix} * \bar{y}_i(1) \qquad (15)$$

$$\mathbf{Gy_i} = \begin{bmatrix} -1 & -2 & -1 \\ 0 & 0 & 0 \\ 1 & 2 & 1 \end{bmatrix} * \bar{y}_i(1). \qquad (16)$$

3) The local Shannon entropy E_i is computed over G_i using (8), as shown in Fig. 6(c).

4) The local Shannon entropy map is binarized by assuming that $E_i \rightarrow 0$ on sky regions, as shown in Fig. 6(d).

$$\bar{E}_i = \begin{cases} 0, & \text{if } E_i < \text{entropy\_threshold} \\ 1, & \text{otherwise.} \end{cases} \qquad (17)$$

5) The dark channel map is binarized considering that on sky regions $dc_i^1 \rightarrow 1$, as depicted in Fig. 6(e) and 6(f).

$$\bar{dc}_i^1 = \begin{cases} 1, & \text{if } dc_i^1 > dc \text{ threshold} \\ 0, & \text{otherwise.} \end{cases} \qquad (18)$$

6) A baseline sky segmentation S_i is obtained by combining $\bar{E}_i$ and $\bar{dc}_i^1$ through the AND logical operator ($\wedge$), (19), as shown in Fig. 6(g).

$$S_i = \bar{E}_i \wedge \bar{dc}_i^1. \qquad (19)$$

- Stage 2. Refine and improve sky region S_i through morphological operations.

7) In order to obtain the basic structure of S_i, its morphological skeleton sk_i^0 must be computed, as depicted in Fig. 6(h).

8) Seeds sd_i are obtained for a region growing process by computing and combining the skeleton branches and endpoints through the OR logical operator ($\vee$), [39] of sk_i^0 as shown in Fig. 6(i).

$$sd_i = \text{get\_branches}(sk_i^0) \vee \text{get\_endpoints}(sk_i^0). \qquad (20)$$

Stage 1

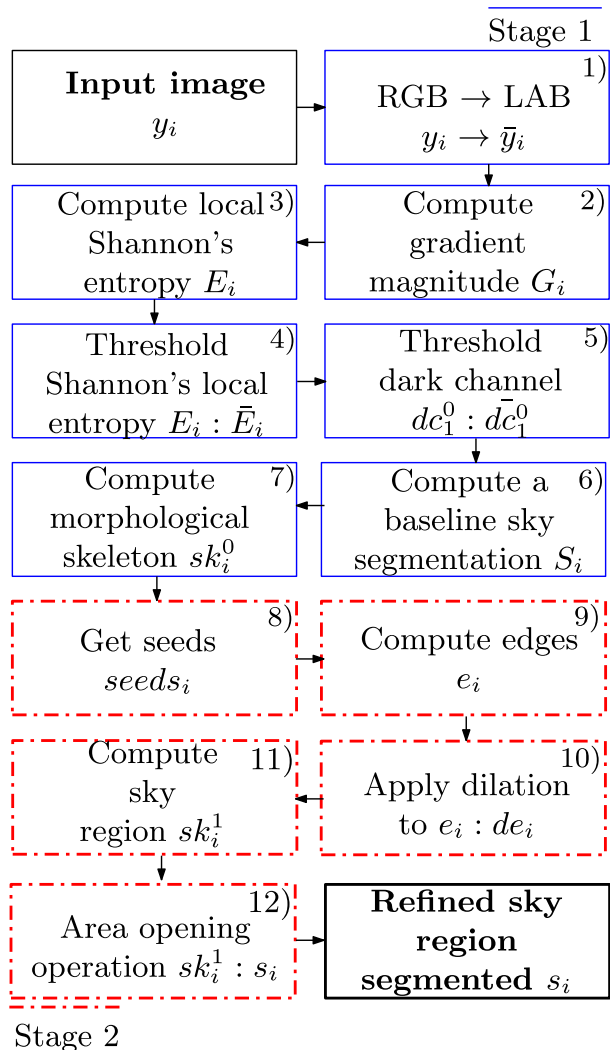|	
Input image y_i	1) RGB → LAB $y_i \rightarrow \bar{y}_i$
Compute local 3) Shannon's entropy E_i	2) Compute gradient magnitude G_i
Threshold 4) Shannon's local entropy $E_i : \bar{E}_i$	Threshold 5) dark channel $dc_1^0 : \bar{dc}_1^0$
Compute 7) morphological skeleton sk_i^0	Compute a 6) baseline sky segmentation S_i
Get seeds 8) $seeds_i$	Compute edges 9) e_i
Compute 11) sky region sk_i^1	Apply dilation 10) to $e_i : de_i$
Area opening 12) operation $sk_i^1 : s_i$	**Refined sky region segmented** s_i

Stage 2

FIGURE 5. **Flowchart for the sky detection-segmentation process. Stage 1: detection and segmentation of a base line sky region. Stage2: refinement of the sky segmentation region.**

9) Compute image e_i by binarizing G_i using an edge threshold as illustrated in Fig. 6(j).

$$e_i = \begin{cases} 1, & \text{if } G_i > \text{edge\_threshold} \\ 0, & \text{otherwise.} \end{cases} \qquad (21)$$

10) In order to avoid possible discontinuities in e_i, a morphological dilation is applied on e_i using a structural element B, as displayed in Fig. 6(k).

$$de_i = \delta_B(e_i). \qquad (22)$$

11) Remove false edges by applying an AND ($\wedge$) operation between $\bar{dc}_i^0$ and de_i

$$de_i = de_i \wedge \bar{dc}_i^0. \qquad (23)$$

12) Region growing [40] is used for computing the accurate sky region. Region growing examines

neighboring pixels of initial seed points sd_i stopping when an edge in de_i is found, as depicted in Fig. 6(l), 6(m), and 6(n).

$$sk_i^1 = \text{region\_growing}(sd_i, de_i). \qquad (24)$$

13) False sky regions are removed by applying a morphological opening operation [41], as shown in Figure 6(o)

$$s_i = \text{area\_opening}(sk_i^1). \qquad (25)$$

Please see Fig. 6(o).

The parameters of the proposed method were tuning empirically, using the images in the dataset [42]. The code of the proposed method can be found in.[3]

C. SKY DETECTION-SEGMENTATION STAGE VALIDATION

Since the proposed method aims to diminish haze effects on outdoor images using a sky detection-segmentation stage, it is necessary to measure the performance of this stage; hence, the dataset in [43] was used, which is a 60-images subset with the corresponding ground-truth from Caltech Airplanes Side dataset [44]. A Jaccard similarity coefficient was used for measuring the segmentation quality, which is a commonly used metric in the literature [45] and it is defined as the size of the intersection between two finite sets divided by the size of their junction, multiplied by 100. That is:

$$J(A, B) = \frac{|A \cap B|}{|A \cup B|} \times 100 \qquad (26)$$

The Jaccard index defines a similarity percentage between 0 and 100. The median Jaccard index reached by the detection-segmentation stage in this work was 96.24 %, which validates the applied method. Fig. 7 shows two examples from the used database and the corresponding results obtained through the proposed approach.

D. DATA

The quantitative evaluation of the proposed algorithm is performed using the following datasets, in order to have a wide range of images for testing. It is worth it to notice that these datasets were used in recent works from reviewed literature.

- Hybrid Subjective Testing Set (HSTS) from a Realistic Single Image Dehazing (RESIDE) dataset composed of ten real-world images [33].
- Synthetic Objective Testing Set (SOTS) from a Realistic Single Image Dehazing (RESIDE) dataset composed of 500 synthetic images [33].
- A HazeRD dataset composed of 14 real-world images, in which the haze was simulated with different visual ranges (0.05, 0.1, 0.2, 0.5, and 1 Km) [34].

Only outdoor images from the above datasets are used to evaluate the proposed method, allowing an accurate simulation of fog with realistic parameters, which are justified by the scattering theory. The parameter ω from (6) used in the experiments of our method is 0.95.
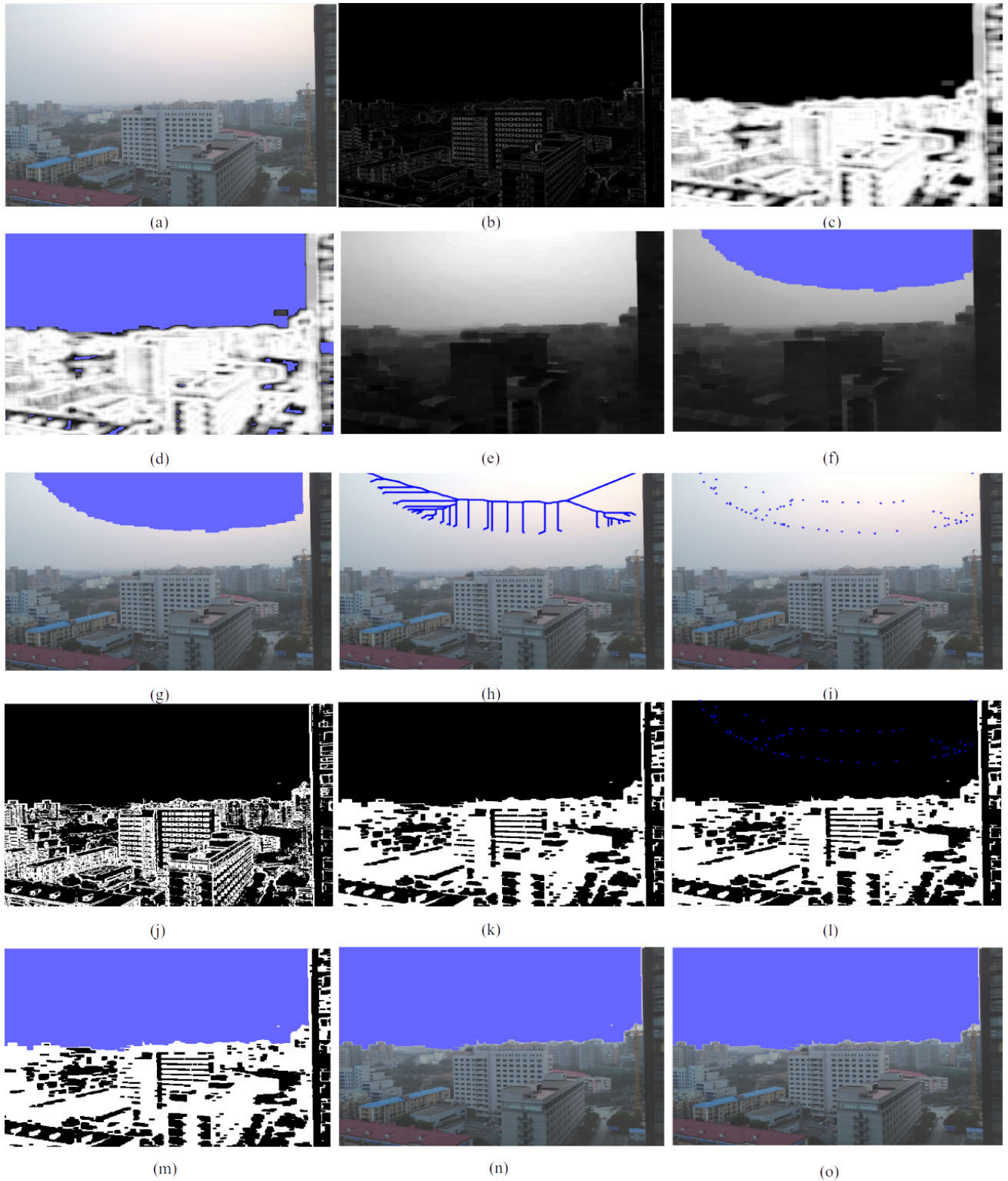
[3]Link to code via github

FIGURE 6. Sky detection-segmentation process. (a) Input image y_i, (b) gradient magnitude G_i, (c) local Shannon entropy E_i, (d) binarized local Shannon entropy $\bar{E}_i$, (e) dark channel dc_1^0, (f) binarized dark channel $\bar{d}c_1^0$, (g) segmented baseline sky S_i, (h) morphological skeleton sk_i^0, (i) obtained seeds sd_i, (j) estimated edges e_i, (k) dilated edges de_i, (l) $de_i^s d_i$, (m) segmented sky region sk_i^1, (n) segmented sky region sk_i^1 over the input image y_i, (o) refined sky segmented s_i.

E. QUANTITATIVE EVALUATION

1) PERFORMANCE METRICS

Full reference metrics PSNR and SSIM, as well as the no-reference metric NIQE were used for evaluating and comparing quantitatively the proposed-method performance. These metrics are described as follows:

- The Peak Signal-to-Noise Ratio (PSNR) is a quantitative measure about the quality of a reconstruction. This is one of the most widely used metrics in dehazing literature [46]. The mean square error (MSE) between two $m \times n$ monochromatic images I and J is required to obtain the PSNR metric, as follows:

$$\text{MSE} = \frac{1}{mn} \sum_{i=0}^{m-1} \sum_{j=0}^{n-1} ||I(i,j) - J(i,j)||^2; \quad (27)$$

hence, the PSNR is given by

$$\text{PSNR} = 10 \log_{10}\left(\frac{\text{MAX}_I^2}{\text{MSE}}\right) = 20 \log_{10}\left(\frac{\text{MAX}_I}{\sqrt{\text{MSE}}}\right), \quad (28)$$

where $\text{MAX} = 2^B - 1$ and B is the number of bits used in the image. The higher the PSNR value, the better the restoration.

- Structural Similarity (SSIM) Index is a perceptual image-similarity metric, alternative to the mean square error MSE) and PSNR, to increase correlation with subjective assessment. For an original and a reconstructed image, I and J, respectively, SSIM is defined as

$$\text{SSIM}(I,J) = \frac{(2\mu_I\mu_J + C_1)(2\sigma_{IJ} + C_2)}{(\mu_I^2 + \mu_J^2 + C_1)(\sigma_I^2 + \sigma_J^2 + C_2)}, \quad (29)$$

where μ, σ and σ_{IJ}, are the mean, the variance, and covariance of the images, respectively.

- Naturalness Image Quality Evaluator (NIQE) [47] is a no-reference, image-quality score, which is based on the construction of "quality-aware" features and their adaptation to a Multivariate Gaussian (MVG) model. The quality-aware characteristics are derived from a Natural Scene Statistics (NSS) model. Quality is expressed as the distance between the MVG and NSS elements extracted from the assessed image, and the corresponding MVG quality characteristics obtained from the natural image corpus.

IV. RESULTS AND ANALYSIS

Quantitative and qualitative tests are performed to evaluate and compare the efficiency of the proposed method, using metrics as in [11], [48], and [16], [49] for its assessment. The quantitative evaluation is performed through the commonly used PSNR value and SSIM index to determine the recovered-image quality as in [5]–[7], [19], [33].

All experiments and tests were performed on a PC with 2.6 GHz Intel Core *i*7-6700HQ, Nvidia GTX 950m GPU and 16 GB of RAM. All methods except the one proposed by Qu *et al.* [20] are Matlab2018-coded and run using only the
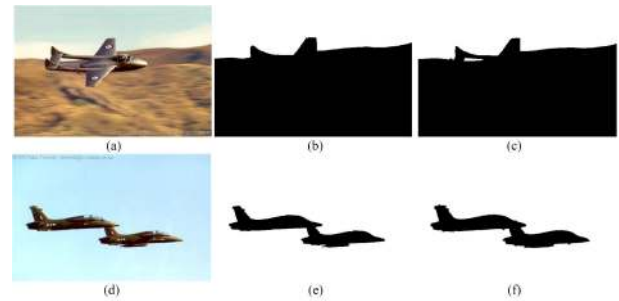

FIGURE 7. Two samples from the database used for assessing the sky detection-segmentation stage. (a), (d) Input image, (b), (e) ground-truth sky mask, (c), (f) proposed-method output mask.

CPU. The Qu *et al.* [20] method runs on Python 3 language and Caffe framework using the GPU (4 GB RAM).

A. QUALITATIVE EVALUATION

Fig. 8 shows 10-real world images from the HSTS dataset; where column (a) represents the ground-truth images, column (b) represents synthetic fogged images, and (c) to (k) depict the results from different defogging algorithms: (c) He *et al.* [7], (d) Pang *et al.* [11], (e) Zhu and He [10], (f) Berman *et al.* [13], (g) Ren *et al.* [17], (h) Cai *et al.* [18], (i) Li *et al.* [19], (j) Salazar-Colores *et al.*, [16], and (k) Qu *et al.* [20]. Columns (l) shows the result from the proposed method. From this figure, it can be observed that the algorithms (c), (e), and (g) show unreal colors in the retrieved image, mainly in the sky region; moreover, methods (e), (f), (g) and (i) present some visual artifacts in zones with different depth values.

Fig. 9 shows 5 out of 500 real-world outdoor images from the SOTS dataset. These ground-truth images are depicted in column (a). Fog-affected images are shown in column (b), and the image-restoration results are listed in subsequent columns as follows: (c) He *et al.* [7], (d) Pang *et al.* [11], (e) Zhu and He [10], (f) Berman *et al.* [13], (g) Ren *et al.* [17], (h) Cai *et al.* [18], (i) Li *et al.* [19], (j) Salazar-Colores *et al.* [16], and (k) Qu *et al.* [20]. Column (l) shows the result from the proposed method.

These results are consistent with those shown in Fig. 8. Similar changes can be seen in the color of sky regions when methods (c), (e), (f), and (g) are used; furthermore, some artifacts are present by using methods (e), (f), (g), and (i).

B. QUANTITATIVE EVALUATION

As described before, SSIM index is computed over the restored images shown in Fig. 8, obtaining the corresponding index values given in Table 1.

The results are compared against the nine methods, demonstrating that the proposed method can achieve a SSIM index of 0.9, which is the second one average index of the compared methods, only Qu *et al.* [20] shows better performance. Note that Cai *et al* [18]. and Li *et al.* [19] use a deep-learning technique, which is a state-of-art method, whereas the other methods show lesser SSIM index values. The SSIM index
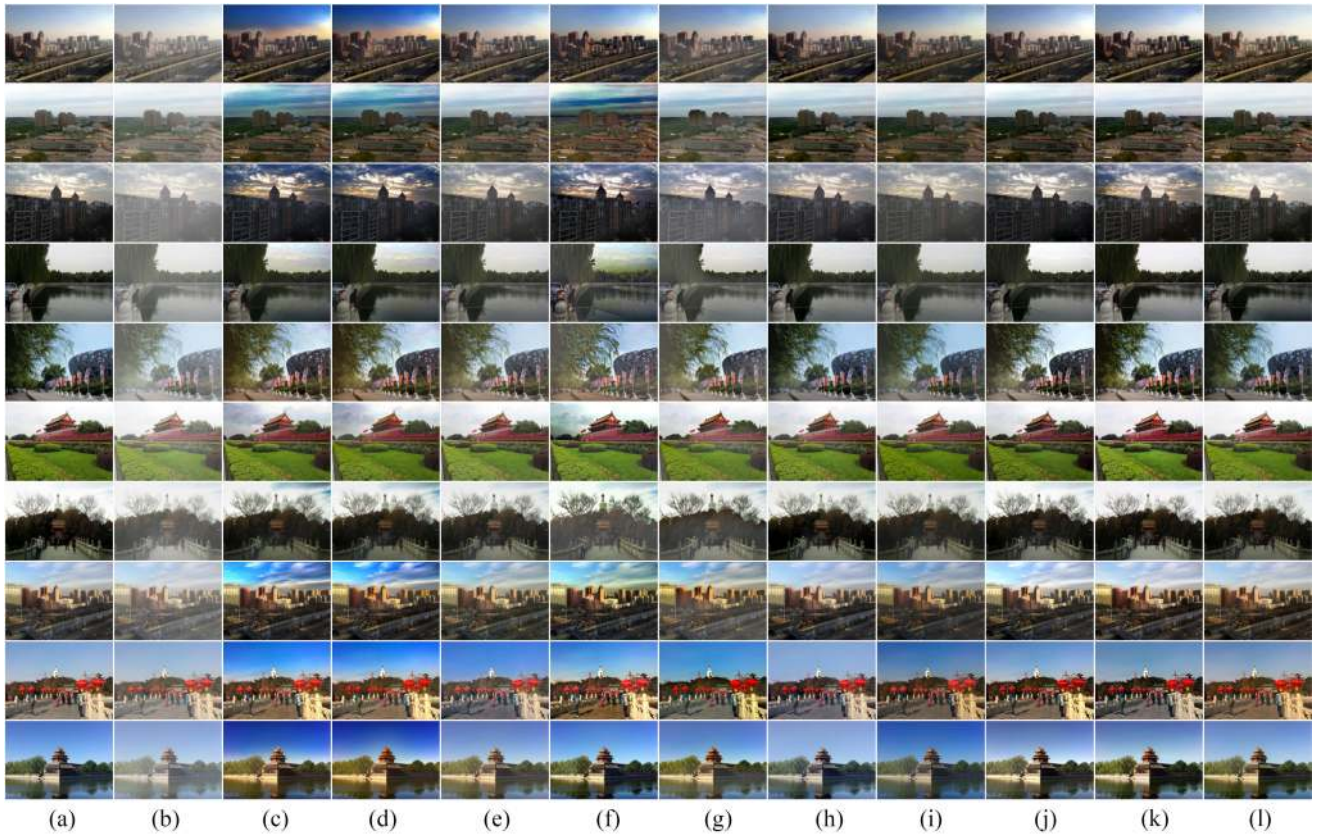
FIGURE 8. Qualitative comparison of ten images from HSTS dataset using different algorithms. (a) ground-truth images, (b) images with fog, (c) He *et al.* method, (d) Pang *et al.* method, (e) Zhu *et al.* method, (f) Berman *et al.* method, (g) Ren *et al.* method, (h) Cai *et al.* method, (i) Li *et al.* method, (j) Salazar *et al.*, (k) Qu *et al.*, and (l) proposed method.

TABLE 1. SSIM index from the 10 images from HSTS dataset presented at Fig. 8 and numeric comparison with different defogging methods.

Image ID	He et al	Pang et al.	Zhu et al.	Berman et al.	Ren et al.	Cai et al.	Li et al.	Salazar et al.	Qu et al.	Proposed method
586	0.82	0.82	0.92	0.88	0.88	0.91	**0.94**	0.91	0.92	0.93
1352	0.80	0.80	**0.93**	0.77	0.91	0.87	**0.93**	0.84	0.92	0.91
1381	0.83	0.83	0.82	0.86	0.70	0.88	0.80	0.90	**0.93**	0.92
3146	0.76	0.77	0.78	0.65	0.73	0.87	0.83	0.85	**0.95**	0.85
4184	0.79	0.80	0.78	0.70	0.74	0.86	0.85	0.82	**0.93**	0.86
4561	0.81	0.81	0.83	0.81	0.80	0.85	**0.95**	0.85	0.94	0.88
5576	0.75	0.79	0.78	0.65	0.68	0.84	0.83	0.84	**0.92**	0.86
5920	0.84	0.85	0.93	0.88	0.87	0.92	**0.94**	0.90	**0.94**	0.91
7471	0.85	0.84	0.89	0.87	0.85	0.93	0.89	0.89	**0.92**	**0.92**
8180	0.83	0.83	0.91	0.92	0.91	**0.93**	0.91	0.91	**0.93**	0.92
Average	0.81	0.82	0.86	0.80	0.81	0.89	0.89	0.87	**0.93**	0.90

TABLE 2. PSNR from the 10 images from HSTS dataset presented at Fig. 8 and numeric comparison with different defogging methods.

Image ID	He et al	Pang et al.	Zhu et al.	Berman et al.	Ren et al.	Cai et al.	Li et al.	Salazar et al.	Qu et al.	Proposed method
586	13.57	13.64	20.82	18.58	19.37	22.58	19.47	22.22	21.47	**27.22**
1352	13.06	13.04	21.65	11.46	20.04	19.87	20.44	18.29	22.52	**23.54**
1381	14.93	14.95	19.92	16.86	14.28	22.86	18.57	22.95	19.99	**24.96**
3146	18.91	19.04	21.41	15.13	17.28	26.69	21.68	23.99	**27.71**	20.02
4184	20.99	21.19	18.43	15.14	16.25	23.69	19.44	19.72	23.29	**23.84**
4561	20.10	20.00	22.36	19.18	20.82	24.77	**29.23**	25.26	28.20	26.87
5576	19.35	20.82	21.75	14.56	16.26	23.57	20.61	23.46	**26.35**	25.11
5920	18.85	18.98	26.93	20.80	20.52	**28.46**	21.67	24.52	25.91	27.10
7471	18.23	18.48	19.60	19.70	18.22	**26.00**	15.78	21.65	20.10	22.58
8180	16.48	16.85	22.85	**24.72**	24.08	22.67	19.01	22.88	23.40	23.66
Average	17.45	17.70	21.57	17.61	18.71	24.12	20.59	22.49	23.89	**24.49**

results appear to be in good agreement with the visual evaluation presented in Fig. 8 and with the results shown in Fig. 10.

The PSNR computations using the 10 HSTS images overall methods are presented in Table 2. These results revealed that the proposed method has a significant advantage over the other methods; only the method reported by Cai *et al.* [18] has a similar PSNR value. The obtained experimental results corroborate that the method proposed in this work provides a similar or even a better outcome than those in the state-of-the-art, including artificial intelligence methods, considering PSNR value and SSIM index.

The SSIM index was computed for over 500 images from SOTS to statistically evaluate and compare the proposed method against the other nine approaches. The results are presented using a *box-plot*. See Fig. 10. The *box-plot* is divided into four parts (quartiles), where the red central line represents the median value. By comparing the median values of the SSIM index, it is possible to note that the proposed method is one of the best three methods (higher SSIM). By comparing the interquartile range (the box), it is possible to see that our method returns the most compact interquartile range, meaning that it is robust. Additionally, this method
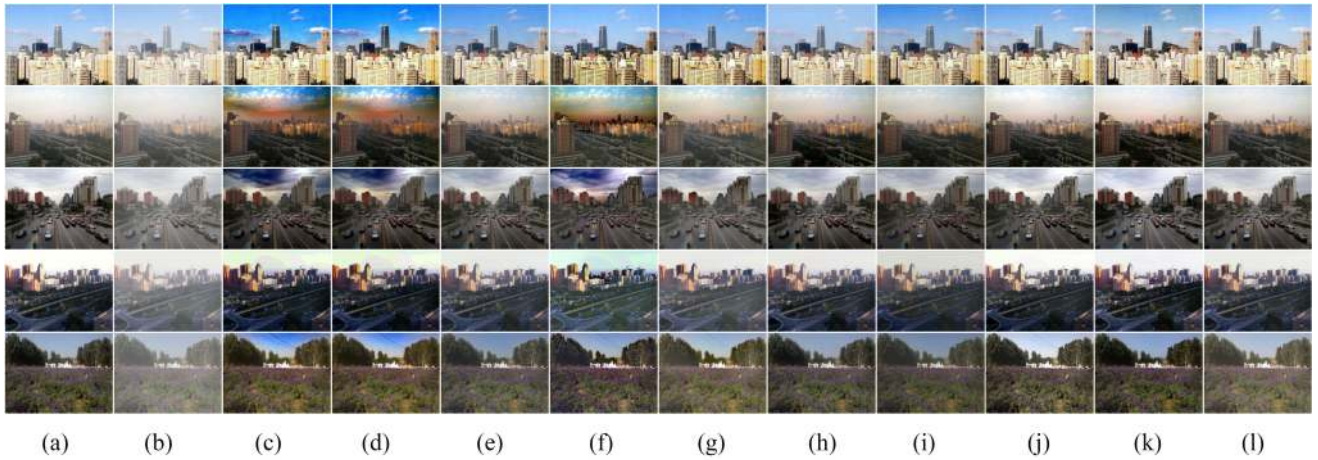
FIGURE 9. Qualitative comparison example of 5 images from RESIDE dataset. (a) Ground-truth images, (b) images with fog, (c) He *et al.* method, (d) Pang *et al.* method, (e) Zhu *et al.* method, (f) Berman *et al.* method, (g) Ren *et al.* method, (h) Cai *et al.* method, (i) Li *et al.* method, (j) Salazar *et al.*, (k) Qu *et al.*, and (l) proposed method.
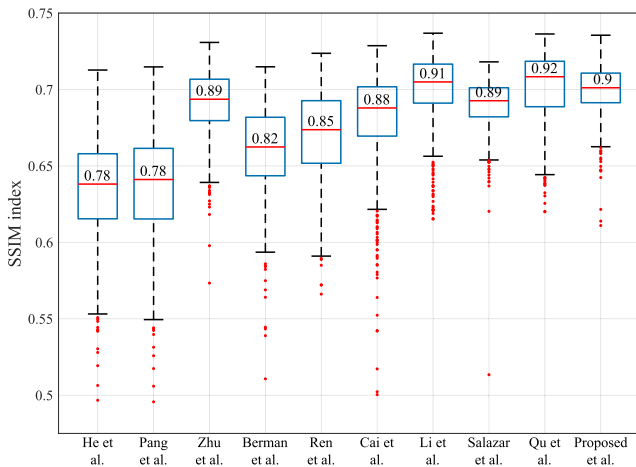

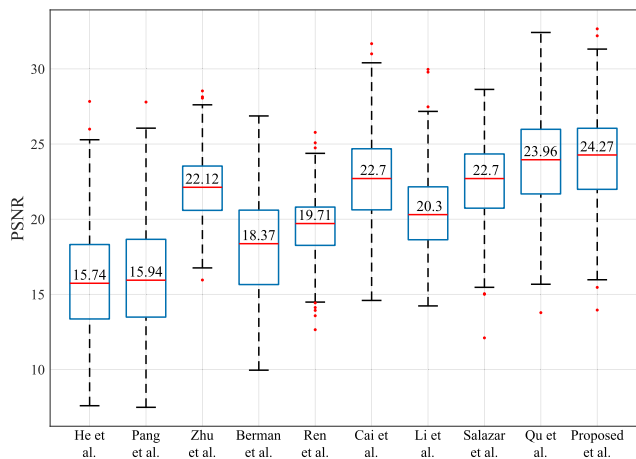**FIGURE 10.** Box-plot comparison of the SSIM index using 500 outdoor from SOTS dataset.

FIGURE 11. Method comparison in terms of PSNR, over 500 outdoor real-world images obtained from SOTS dataset.
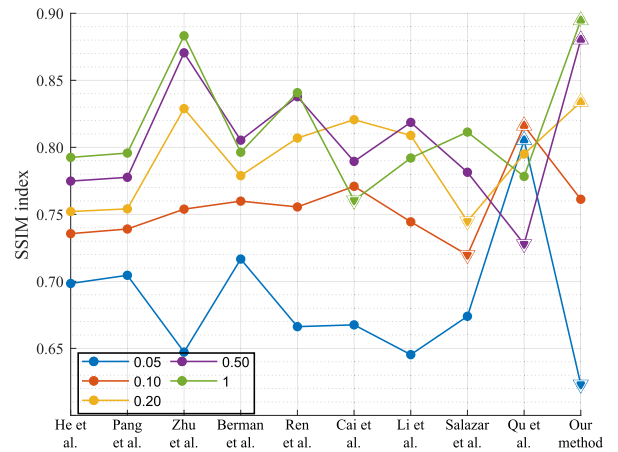

FIGURE 12. Comparison of the average SSIM index for retrieved images from pictures of the HazeRD dataset with different visibility ranges.
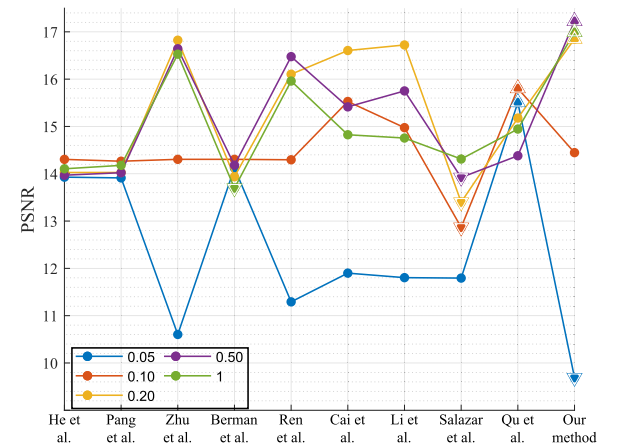
FIGURE 13. Comparison of the average PSNR value for retrieved images from pictures of the HazeRD dataset with different visibility ranges.

can generalize better than the AI-based methods. Finally, those points outside of the *whiskers* represent outliers.[4]

---

[4]Outlier points are defined as the points outside 1.5 times the interquartile range above the upper quartile and below the lower quartile.

The performance of classical DCP and FGF approach, considering the SSIM index, is consistently lower than the proposed method.

FIGURE 14. Example of HazeRD image with different visibility haze conditions. (a) Ground-truth image, (b) 1km, (c) 0.50 km, (d) 0.20 km, (e) 0.10 km, and (f) 0.05 km.
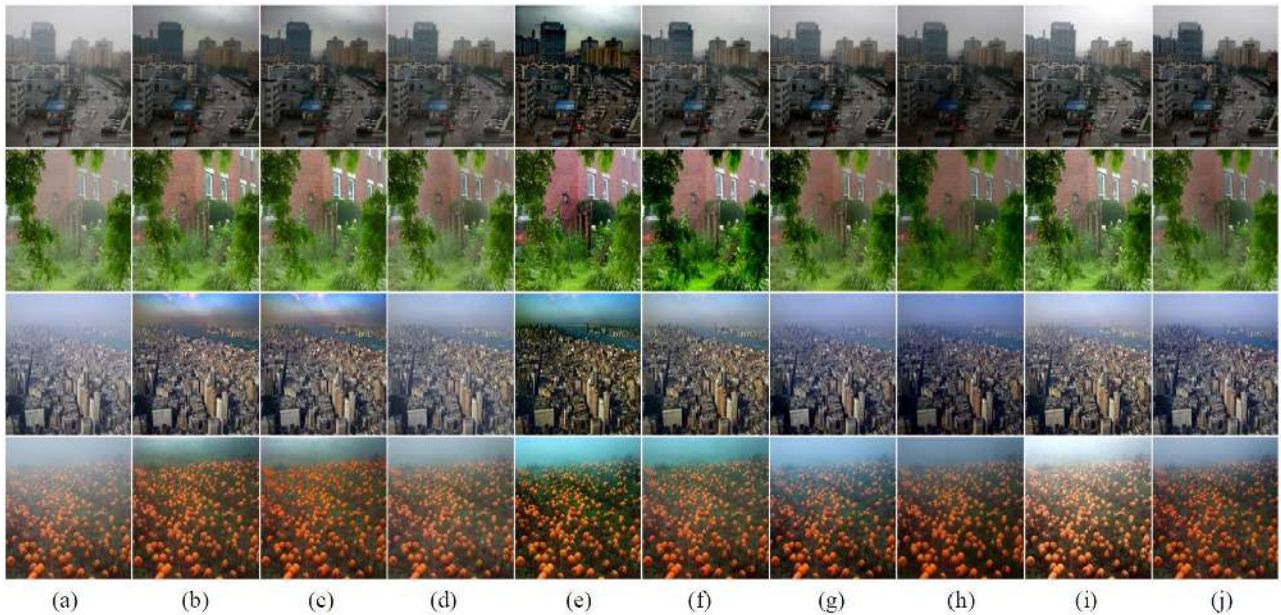

FIGURE 15. Qualitative comparison example of 4 images from literature. (a) Images with fog, (b) He *et al.* method, (c) Pang *et al.* method, (d) Zhu *et al.* method, (e) Berman et. al. method, (f) Ren *et al.* method, (g) Cai *et al.* method, (h) Li *et al.* method, (i) Salazar *et al.*, (j) Qu *et al.*, and (k) proposed method.

Similarly, the PSNR computation over the 500 images from SOTS dataset is illustrated through *box-plots* in Fig. 11. In general, it is possible to see that the PSNR range value is higher than the SSIM index. The proposed method has the best median value 24.27. By comparing the inter-quartile range, it is possible to see that Zhu *et al.*, Cai *et al.*, Li *et al.*, Salazar *et al.*, Qu *et al.* and the proposed method have similar performance. Compared against the DCP-based/FGF methods, He *et al.* and Pang *et al.*, the proposed-method performance, using this metric, is remarkably higher.

Another dataset used for the quantitative evaluation was the HazeRD dataset [34]. The quantitative evaluation is based on the SSIM index and PSNR over the same outdoor images with 5 different visual ranges: 0.05 km, 0.10 km, 0.20 km, 0.50 km, and 1 km, where 0.05 km is the highest fog density and the lowest visual range. Fig. 14 presents an example of an image with different fog intensities.

Fig. 12 presents the SSIM index over five visual ranges: 0.05 km, 0.10 km, 0.20 km, 0.50 km, 1 km, and the average, using the HazeRD dataset. The point-up triangle marker ($\triangle$) represents the maximum SSIM index over all methods at certain visual range. In contrast, the point-down triangle marker (∇) represents the minimum index over all methods. Fig. 14 reveals that our method has outstanding performance in the

visual ranges of 0.20 km, 0.50 km, 1 km, and the average value. These results suggest that the defogging methods, including the deep-learning techniques (e.g. Cai *et al.* [18], Li *et al.* [50], and Ren *et al.* [17]), have a lower SSIM performance with different illumination and contrast conditions. Although the SSIM performance of our method is not the best at 0.05 and 0.10 km, it exhibits a superior SSIM performance to the remaining methods.

Average PSNR values for the retrieved images from the HazeRD dataset are shown in Fig. 13, over the five visual ranges: 0.05 km, 0.10 km, 0.20 km, 0.50 km, 1 km. From this figure, the proposed method shows the best performance with the highest PSNR value, indicated by the pointing-up triangular marker (($\triangle$)), at 0.50 km, 0.20 km and 1 km.

Four real-world images (Fig. 15) widely used in the literature were employed to evaluate the methods performance with the no-reference metric NIQE. From obtained results, the proposed method achieves the second-best outcome, being outperformed just by the Zhu *et al.* method; however, this approach shows an inferior performance than the proposed method considering PSNR and SSIM metrics. Finally, the AI-based methods have worse performance than the classical methods in all cases.

TABLE 3. NIQE metric values results (less is best).

Image ID	Input	He et al	Pang et al.	Zhu et al.	Berman et al.	Ren et al.	Cai et al.	Li et al.	Salazar et al.	Qu et al.	Proposed method
City_1	2.21	2.19	**2.07**	2.21	2.65	2.23	2.28	3.84	2.33	2.49	2.15
House	2.83	3.12	3.27	2.82	3.58	3.61	2.96	3.51	3.33	**3.82**	2.95
Ny_2	2.57	2.72	2.75	2.58	2.83	2.56	2.59	3.85	2.55	**2.48**	2.59
Pumpkins	3.73	**2.74**	3.26	2.92	3.44	3.46	2.97	2.76	3.09	3.89	3.03
Average	2.83	2.69	2.84	**2.63**	3.12	2.96	2.70	3.49	2.82	3.17	2.68

TABLE 4. Elapsed-time comparison for different defogging algorithms in seconds, considering different resolutions.

Image Size	He et al.	Pang et al.	Zhu et al.	Berman et al.	Ren et al.	Cai et al.	Li et al.	Salazar et al.	Qu et al.	Proposed method
640 × 480	22.96	3.33	0.73	1.63	1.64	3.72	1.14	0.57	**0.0008**	0.57
800 × 600	35.58	4.91	1.02	2.20	2.28	5.81	1.85	0.82	**0.001**	0.68
1024 × 768	67.75	7.91	1.60	3.69	4.75	10.15	3.03	1.56	**0.004**	1.02
1280 × 720	76.08	9.51	1.64	4.16	4.13	11.61	3.42	1.54	**0.004**	1.06
1920 × 1080	194.1	21.77	3.85	9.87	10.46	23.8	9.4	3.36	error[5]	**1.78**

C. PROCESSING TIME

In Table 4, a time-consumption comparison is performed considering all methods with different image resolutions (640 × 480, 800 × 600, 1024 × 768, 1280 × 720, 1920 × 1080). From this table, it is worth it to notice that the proposed method has the lowest processing time in comparison to all the other approaches with similar software and hardware conditions, considering all image resolutions. The Qu *et al.* method [20] a faster processing time; however, it could not be considered a fair comparison since, the method is implemented on Python, and executed using GPUs. Moreover, it is important to notice that with the maximum image size (1920 × 1080) considered in this work, this method deliver a memory error; therefore, it can be considered that a very important feature of the proposed method is its capability of being implemented in conventional embedded systems, making it suitable for being used in real-life, computer-vision applications to carry out defogging tasks online.

V. CONCLUSION

Defogging is a significant process of computer vision, which has to consider several factors like restoration quality, different fog-intensity scenarios (visual ranges), and processing time. DCP is usually employed for this task; however, it suffers from high time-consumption, artifact generation, and sky-region over-saturation; hence, resent research has focused on improving these features in dehazing methods. In this research, the recovery of a sharp image from its hazy version, eluding the DCP limitations, is aimed. The proposed method performance is assessed through a qualitative and quantitative analysis applying the commonly used SSIM and PSNR metrics over retrieved images from more than 500 pictures of the HSTS, SOTS and HazeRD databases,

and comparing the obtained results against 9 recently proposed approaches in reviewed literature; from there, it is demonstrated that the proposed method falls into the three techniques with the highest SSIM index; furthermore, the it has the highest PSNR median value among all considered defogging approaches. On the other hand, considering different visual ranges, the proposed method shows a superior performance at least in three out of five distinct ranges, than all the other defogging approaches under different illumination and contrast conditions. In addition, the proposed method achieved the second-best performance utilizing the no-reference NIQE metric. Finally, the proposed method has the lowest processing time (under similar conditions of software and hardware), considering different image resolutions, compared to all examined algorithms which is a quite relevant for many computer vision applications.

REFERENCES

[1] B. Li, W. Ren, D. Fu, D. Tao, D. Feng, W. Zeng, and Z. Wang, "Benchmarking single-image dehazing and beyond," *IEEE Trans. Image Process.*, vol. 28, no. 1, pp. 492–505, Jan. 2019.

[2] S. Lee, S. Yun, J.-H. Nam, C. S. Won, and S.-W. Jung, "A review on dark channel prior based image dehazing algorithms," *Eurasip J. Image Video Process.*, vol. 2016, no. 1, p. 4, Dec. 2016.

[3] X. Yan, X. Li, Y. Liu, and J. Zhao, "Effects of foggy conditions on drivers' speed control behaviors at different risk levels," *Saf. Sci.*, vol. 68, pp. 275–287, Oct. 2014.

[4] C. Lee, S. Huh, T. A. Ketter, and M. Unser, "Unsupervised connectivity-based thresholding segmentation of midsagittal brain MR images," *Comput. Biol. Med.*, vol. 28, no. 3, pp. 309–338, May 1998.

[5] W. Wang, X. Yuan, X. Wu, and Y. Liu, "Fast image dehazing method based on linear transformation," *IEEE Trans. Multimedia*, vol. 19, no. 6, pp. 1142–1155, Jun. 2017.

[6] C. Chengtao, Z. Qiuyu, and L. Yanhua, "A survey of image dehazing approaches," in *Proc. 27th Chin. Control Decis. Conf. (CCDC)*, May 2015, pp. 3964–3969.

[7] K. He, J. Sun, and X. Tang, "Single image haze removal using dark channel prior," *IEEE Trans. Pattern Anal. Mach. Intell.*, vol. 33, no. 12, pp. 2341–2353, Dec. 2011.

[8] Y.-B. Zhu, J.-M. Liu, and Y.-G. Hao, "An single image dehazing algorithm using sky detection and segmentation," in *Proc. 7th Int. Congr. Image Signal Process.*, Oct. 2014, pp. 248–252.

[9] H. Yuan, C. Liu, Z. Guo, and Z. Sun, "A region-wised medium transmission based image dehazing method," *IEEE Access*, vol. 5, pp. 1735–1742, 2017.

[10] M. Zhu and B. He, "Dehazing via graph cut," *Opt. Eng.*, vol. 56, pp. 113105–113111, 2017.

[11] J. Pang, A. Oscar, and G. Zheng, "Improved single image dehazing using guided filter," in *Proc. APSIPA Annu. Summit Conf. (APSIPA ASC)*, Xi'an, China, vol. 1, Oct. 2011, pp. 1–4.

[12] K. Nishino, L. Kratz, and S. Lombardi, "Bayesian defogging," *Int. J. Comput. Vis.*, vol. 98, no. 3, pp. 263–278, Jul. 2012.

[13] D. Berman, T. Treibitz, and S. Avidan, "Non-local image dehazing," in *Proc. IEEE Conf. Comput. Vis. Pattern Recognit. (CVPR)*, Jun. 2016, pp. 1674–1682.

[14] Q. Shu, C. Wu, Q. Zhong, and R. W. Liu, "Alternating minimization algorithm for hybrid regularized variational image dehazing," *Optik*, vol. 185, pp. 943–956, May 2019.

[15] R. W. Liu, S. Xiong, and H. Wu, "A second-order variational framework for joint depth map estimation and image dehazing," in *Proc. IEEE Int. Conf. Acoust., Speech Signal Process. (ICASSP)*, Apr. 2018, pp. 1433–1437.

[16] S. Salazar-Colores, I. Cruz-Aceves, and J.-M. Ramos-Arreguin, "Single image dehazing using a multilayer perceptron," *J. Electron. Imag.*, vol. 27, pp. 43011–43022, 2018.

---

[5]Runtime error: CUDA out of memory.

[17] W. Ren, S. Liu, H. Zhang, J. Pan, X. Cao, and M.-H. Yang, "Single image dehazing via multi-scale convolutional neural networks," in *Computer Vision—ECCV*, B. Leibe, J. Matas, N. Sebe, and M. Welling, Eds. Cham, Switzerland: Springer, 2016, pp. 154–169.

[18] B. Cai, X. Xu, K. Jia, C. Qing, and D. Tao, "DehazeNet: An end-to-end system for single image haze removal," *IEEE Trans. Image Process.*, vol. 25, no. 11, pp. 5187–5198, Nov. 2016.

[19] B. Li, X. Peng, Z. Wang, J. Xu, and D. Feng, "AOD-Net: All-in-One dehazing network," in *Proc. IEEE Int. Conf. Comput. Vis. (ICCV)*, Oct. 2017, pp. 4780–4788.

[20] Y. Qu, Y. Chen, J. Huang, and Y. Xie, "Enhanced Pix2pix dehazing network," in *Proc. IEEE/CVF Conf. Comput. Vis. Pattern Recognit. (CVPR)*, Jun. 2019, pp. 8160–8168.

[21] H. Fu, B. Wu, and Y. Shao, "Multi-feature-based bilinear CNN for single image dehazing," *IEEE Access*, vol. 7, pp. 74316–74326, 2019.

[22] M. Zhu, B. He, J. Liu, and L. Zhang, "Dark channel: The devil is in the details," *IEEE Signal Process. Lett.*, vol. 26, no. 7, pp. 981–985, Jul. 2019.

[23] Y. Liu, H. Li, and M. Wang, "Single image dehazing via large sky region segmentation and multiscale opening dark channel model," *IEEE Access*, vol. 5, pp. 8890–8903, 2017.

[24] W. Wang, X. Yuan, X. Wu, and Y. Liu, "Dehazing for images with large sky region," *Neurocomputing*, vol. 238, pp. 365–376, May 2017.

[25] H. Fu, B. Wu, Y. Shao, and H. Zhang, "Scene-awareness based single image dehazing technique via automatic estimation of sky area," *IEEE Access*, vol. 7, pp. 1829–1839, 2019.

[26] H. Fu, B. Wu, Y. Shao, and H. Zhang, "Perception oriented haze image definition restoration by basing on physical optics model," *IEEE Photon. J.*, vol. 10, no. 3, pp. 1–16, Jun. 2018.

[27] R. Fattal, "Dehazing using color-lines," *ACM Trans. Graph.*, vol. 34, no. 1, pp. 13:1–13:14, Dec. 2014.

[28] X. Min, G. Zhai, K. Gu, Y. Zhu, J. Zhou, G. Guo, X. Yang, X. Guan, and W. Zhang, "Quality evaluation of image dehazing methods using synthetic hazy images," *IEEE Trans. Multimedia*, vol. 21, no. 9, pp. 2319–2333, Sep. 2019.

[29] C. O. Ancuti, C. Ancuti, R. Timofte, L. Van Gool, L. Zhang, and M.-H. Yang, "NTIRE 2019 image dehazing challenge report," in *Proc. IEEE/CVF Conf. Comput. Vis. Pattern Recognit. Workshops (CVPRW)*, Jun. 2019, pp. 2241–2253.

[30] K. He and J. Sun, "Fast guided filter," 2015, *arXiv:1505.00996*. [Online]. Available: https://arxiv.org/abs/1505.00996

[31] W. Zhang and X. Hou, "Estimation algorithm of atmospheric light based on ant colony optimization," in *Proc. Int. Conf. Intell. Syst., Metaheuristics Swarm Intell. ISMSI*, 2017, pp. 20–25.

[32] A. Galdran, "Image dehazing by artificial multiple-exposure image fusion," *Signal Process.*, vol. 149, pp. 135–147, Aug. 2018.

[33] B. Li, W. Ren, D. Fu, D. Tao, D. Feng, W. Zeng, and Z. Wang, "Benchmarking single-image dehazing and beyond," *IEEE Trans. Image Process.*, vol. 28, no. 1, pp. 492–505, 2018.

[34] Y. Zhang, L. Ding, and G. Sharma, "HazeRD: An outdoor scene dataset and benchmark for single image dehazing," in *Proc. IEEE Int. Conf. Image Process. (ICIP)*, Sep. 2017, pp. 3205–3209.

[35] K. B. Gibson and T. Q. Nguyen, "Fast single image fog removal using the adaptive Wiener filter," in *Proc. IEEE Int. Conf. Image Process.*, Sep. 2013, pp. 714–718.

[36] K. He, J. Sun, and X. Tang, "Single image haze removal using dark channel prior," Ph.D. dissertation, Dept. Inf. Eng., Chin. Univ. Hong Kong, Hong Kong, 2010.

[37] G. Wang, G. Ren, L. Jiang, and T. Quan, "Single image dehazing algorithm based on sky region segmentation," *Inf. Technol. J.*, vol. 12, no. 6, pp. 1168–1175, Jun. 2013.

[38] P. Ganesan, V. Rajini, and R. I. Rajkumar, "Segmentation and edge detection of color images using CIELAB color space and edge detectors," in *Proc. INTERACT*, Dec. 2010, pp. 393–397.

[39] R. M. Haralick, S. R. Sternberg, and X. Zhuang, "Image analysis using mathematical morphology," *IEEE Trans. Pattern Anal. Mach. Intell.*, vol. PAMI-9, no. 4, pp. 532–550, Jul. 1987.

[40] S. Kamdi and R. K. Krishna, "Image segmentation and region growing algorithm," *Int. J. Comput. Technol. Electron. Eng.*, vol. 2, no. 1, pp. 103–107, 2012.

[41] P. Soille, *Morphological Image Analysis: Principles and Applications*. Santa Clara, CA, USA: Springer, 2013.

[42] M. Sulami, I. Glatzer, R. Fattal, and M. Werman, "Automatic recovery of the atmospheric light in hazy images," in *Proc. IEEE Int. Conf. Comput. Photography (ICCP)*, May 2014, pp. 1–11.

[43] E. B. Alexandre, "IFT-SLIC: Geração de superpixels com base em agrupamento iterativo linear simples e transformada imagem-floresta," Ph.D. dissertation, Universidade de São Paulo, São Paulo, Brazil, 2017.

[44] G. Griffin, A. Holub, and P. Perona, "Caltech-256 object category dataset," California Inst. Technol., Pasadena, CA, USA, Tech. Rep. 2007-001, 2007.

[45] R. Shi, K. N. Ngan, and S. Li, "Jaccard index compensation for object segmentation evaluation," in *Proc. IEEE Int. Conf. Image Process. (ICIP)*, Oct. 2014, pp. 4457–4461.

[46] D. Singh and V. Kumar, "A comprehensive review of computational dehazing techniques," *Arch. Comput. Methods Eng.*, vol. 26, no. 5, pp. 1395–1413, Sep. 2018.

[47] A. Mittal, R. Soundararajan, and A. C. Bovik, "Making a 'completely blind' image quality analyzer," *IEEE Signal Process. Lett.*, vol. 20, no. 3, pp. 209–212, Mar. 2012.

[48] J.-B. Wang, N. He, L.-L. Zhang, and K. Lu, "Single image dehazing with a physical model and dark channel prior," *Neurocomputing*, vol. 149, pp. 718–728, Feb. 2015.

[49] Y. Du, B. Guindon, and J. Cihlar, "Haze detection and removal in high resolution satellite image with wavelet analysis," *IEEE Trans. Geosci. Remote Sens.*, vol. 40, no. 1, pp. 210–217, Jan. 2002.

[50] J. Li, H. Zhang, D. Yuan, and M. Sun, "Single image dehazing using the change of detail prior," *Neurocomputing*, vol. 156, pp. 1–11, May 2015.

SEBASTIÁN SALAZAR-COLORES received the Ph.D. degree in computer science from the Universidad Autónoma de Querétaro, in 2019. He currently works with the Centro de Investigaciones en Óptica, as a Researcher Associate. His research interests include deep learning, computer vision, and signal processing.

E. ULISES MOYA-SÁNCHEZ (Member, IEEE) received the Ph.D. degree from the CINVESTAV Unidad Guadalajara, in 2014. He held a postdoctoral position with the High-Performance Artificial Intelligence Group, Barcelona Supercomputing Center, and is a Researcher with the Universidad Autónoma de Guadalajara. He is a member of the Sistema Nacional de Investigadores (SNI-I), CONACyT, México. He is currently the Artificial Intelligence Director of the Jalisco Government.

JUAN-MANUEL RAMOS-ARREGUÍN (Senior Member, IEEE) received the M.S. degree in electrical engineering option instrumentation and digital systems from the University of Guanajuato and the Ph.D. degree in mechatronics science from the Centro de Ingeniería y Desarrollo Industrial. Since 2009, he has been a part of the Engineering Department, UAQ, where he currently works as a Researcher and Lecturer. His research interests include mechatronics and embedded systems.

EDUARDO CABAL-YÉPEZ (Member, IEEE) received the M.Eng. degree from the Facultad de Ingenieria Mecanica Electrica y Electronica (FIMEE), Universidad de Guanajuato, Mexico, in 2001, and the Ph.D. degree from the University of Sussex, U.K., in 2007. In April 2008, he joined the Division de Ingenierias del Campus Irapuato-Salamanca de la Universidad de Guanajuato, where he is currently a Titular Professor. His current research interests include digital image and signal processing, artificial intelligence, robotics, smart sensors, real-time processing, mechatronics, FPGAs, and embedded systems. He has authored more than 50 articles in international journals and conferences. He is also a National Researcher with the Consejo Nacional de Ciencia y Tecnologia, Mexico.

GERARDO FLORES (Member, IEEE) received the B.S. degree (Hons.) in electronic engineering from the Instituto Tecnológico de Saltillo, Mexico, in 2000, the M.S. degree in automatic control from CINVESTAV-IPN, Mexico City, in 2010, and the Ph.D. degree in systems and information technology from the Heudiasyc Laboratory, Université de Technologie de Compiègne-Sorbonne Universités, France, in 2014. Since 2016, he has been a full-time Researcher and the Head and Founder of the Perception and Robotics Laboratory, Center for Research in Optics, León Guanajuato, Mexico. His research interests include the theoretical and practical problems arising from the development of autonomous and vision systems. He has been a member of the Sistema Nacional de Investigadores, since 2014. He is currently an Associate Editor of *Mathematical Problems in Engineering*.

ULISES CORTÉS is currently a Full-Professor and Researcher of the Universitat Politècnica de Catalunya (UPC). He is the Scientific Coordinator of the High-Performance Artificial Intelligence Group, Barcelona Supercomputing Center (BSC). He works on several areas of artificial intelligence (AI), including knowledge acquisition for and concept formation in knowledge-based systems, as well as on machine learning and in autonomous intelligent agents. He advised 22 Ph.D. Thesis, two of them have been awarded with the ECCAI AI Dissertation Award, and more than 20 Master Thesis in the field of artificial intelligence and has more than 60 articles in international journals and more than 150 papers in conferences and workshops. He is a member of Sistema Nacional de Investigadores (SNI-III), CONACyT, México. In 2018, he was awarded as the Mexicano Distinguido 2018, for his contributions to artificial intelligence by the Instituto de los Mexicanos en el Exterior and Secretaría de Relaciones Exteriores de México.

• • •